Multilevel 2D Bar Codes: Towards High Capacity Storage Modules for Multimedia Security and Management

Renato Villán, Sviatoslav Voloshynovskiy, Oleksiy Koval, and Thierry Pun

Abstract

In this paper, we deal with the design of high-rate multilevel two-dimensional (2D) bar codes for the print-and-scan channel. Firstly, we introduce a framework for evaluating the performance limits of these codes by studying an inter-symbol interference (ISI) free, synchronous, and noiseless print-and-scan channel, where the input and output alphabets are finite and the printer device uses halftoning to simulate multiple gray levels. Secondly, we present a new model for the print-and-scan channel specifically adapted to the problem of communications via multilevel 2D bar codes. This model, inspired by our experimental work, assumes no ISI and perfect synchronization, but independence between the channel input and the noise is not supposed. We adapt the theory of multilevel coding with multistage decoding (MLC/MSD) to the print-and-scan channel. Finally, we present experimental results confirming the utility of our channel model, and showing that multilevel 2D bar codes using MLC/MSD can reliably achieve the high capacity storage requirements of many multimedia security and management applications.

Index Terms

2D bar codes, high capacity storage, print-and-scan channel, multilevel coded modulation.

This work was partially supported by the Swiss National Science Foundation (SNF) professorship grant No. PP002-68653/1, the SNF Interactive Multimodal Information Management (IM2) project, and the European Commission through the programs IST-2002-507932 ECRYPT and FP6-507609 SIMILAR. The information in this document reflects only the authors' views, is provided as is and no guarantee or warranty is given that the information is fit for any particular purpose. The user thereof uses the information at its sole risk and liability.

R. Villán, S. Voloshynovskiy, O. Koval, and T. Pun are with the Stochastic Image Processing Group (http://sip.unige.ch), Department of Computer Science, University of Geneva, 24 rue du Général-Dufour, 1211 Genève 4, Switzerland. The contact author is S. Voloshynovskiy (svolos@cui.unige.ch).

I. INTRODUCTION

Two-dimensional (2D) bar codes are at present widely used in various applications due to their numerous advantages over alternative technologies. Besides being cheap and simple, their main advantage is that they can carry a significant amount of information on surfaces such as paper, plastic, or even ceramics. 2D bar codes can be either directly printed on the above surfaces or engraved using appropriate lasers [1], [2]. Moreover, printing can be performed using either visible, ultraviolet, or infrared inks, depending on the application's concern about security. 2D bar codes can be read using low-resolution readers equipped with cheap charged coupled devices (CCDs) like those in flatbed scanners, handy scanners, digital photo cameras, webcams, or even cell phone cameras.

The wide spread of printing and reading devices makes 2D bar codes a very cheap and attractive technology for various *multimedia management* applications. For example, 2D bar codes are being used in new emerging applications such as *M-ticketing*, where they carry selected information of a ticket that is received via a mobile phone [3]; *digital postage* for online postal services [4]; and *automatic tracing and tracking of printed documents* such as bills, reports, tax forms, etc. Furthermore, since the halftoning printing technique unavoidably leads to the loss in quality of printed documents, 2D bar codes are being considered as an auxiliary channel dedicated to convey additional side information for improving the quality of scanned documents [5].

Another important field where 2D bar codes are used is *multimedia security*. In multimedia security applications, 2D bar codes are mainly considered as an auxiliary channel carrying additional information for *reliable personal identification* [6], *document authentication* and *document tamper proofing*.

In personal identification based on ID documents such as passports, ID cards, driver licences, etc., the *personal information* (name, date and place of birth, nationality), the *document identification data* (document's ID number), and the *personal biometrics* (fingerprint, 2D photo, 3D scan of the head, iris, sample of the voice or other person-dependent data) are properly encoded and stored into a 2D bar code. The purpose of the 2D bar code is twofold. Firstly, it makes the process of information reading from the ID document fast and robust to possible distortions. Secondly, it provides an additional level of security since the personal information can be stored in encrypted form using an appropriate cryptographic asymmetric protocol. In this case, only the authorized private party can encode the information and produce the corresponding 2D bar code. On the other hand, public users can always perform the identification task. Thus, the information stored into the 2D bar code serves as an additional link that connects a person with its physical ID document. Obviously, the storage capacity of the 2D bar code should be adequate to satisfy the above storage requirements and the cryptographic management protocol. Taking into account the growing number of biometrics as well as the particularities of asymmetric encryption protocols, the storage capacity of the 2D bar code should be very high. Alternatively, specific techniques of source coding and feature extraction should be applied to the raw biometric data as well as make use of recent results in elliptic curve encryption in order to reduce the payload that will be stored into the 2D bar code [7]. In many applications, it is also required the 2D bar code to be inseparable or adherent to the document's surface in order to reinforce the link between the physical document and its owner as well as to avoid document duplication. Laser engraving of the 2D bar code seems to be a reasonable solution to this problem.

Document authentication and document tamper proofing aim at guaranteeing the authenticity of a document and at indicating the corresponding modifications, if the document is found to be non-authentic.

The most common solution for document authentication consists in the generation of the document's hash and its protected storage directly onto the document using a 2D bar code. This is the so-called document enrollment procedure. At the authentication stage, the hash is computed again from the document under investigation and compared with the one stored into the 2D bar code. In the case of an authentic document, the two hashes should be identical. Otherwise, the decision about non-authenticity of the document should be declared. Obviously, the hash should be designed accordingly to withstand various unintentional modifications that might occur during the document's life cycle. At the same time, the hash should be sensitive enough to various intentional modifications. The development of such hash functions is an active field of research known as *robust visual hashing* [8].

Contrarily to document authentication, where the hash is taken from the entire document, document tamper proofing is based on the concept of local hashing. The document is divided into a number of parts and a (local) hash is computed from each part. The local hashes are again stored into a 2D bar code. Thus, if some modifications are made to the document, the tamper proofing technology is capable of identifying these modifications locally. This might be useful to provide the interested party with some hints and evidence about the introduced modifications.

It should be also mentioned that the global or local hashes can be stored inside the document itself using digital data-hiding technology, which has some advantages in some specific applications where 2D bar codes are not suitable [9]. However, 2D bar codes are acceptable for many applications and constitute a very attractive solution when the storage capacity of digital data-hiding is too low due to strict constraints imposed on the distortion introduced by this technology or the particularities of some document reproduction and acquisition processes. Moreover, in those applications where the esthetical requirements are of great importance, 2D bar codes can be printed using specific invisible inks or crystals that can be then excited by infrared or ultraviolet light and scanned in the visible range.

The block diagram of document enrollment using a 2D bar code is shown in Fig. 1. The hash is

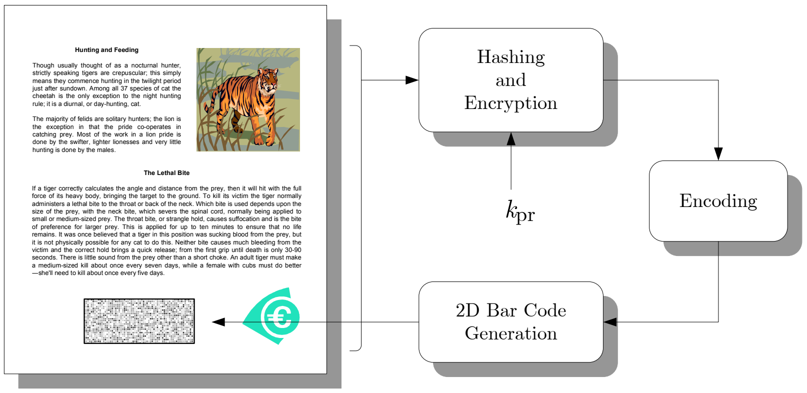

Fig. 1. Document enrollment using a 2D bar code.

computed from the entire document which can include both text, images, logos, drawings, etc. Then, the hash is encrypted using the private key k_{pr} in order to prevent the possibility of generation of a new hash from a tampered version of the document. For the reliable storage into the 2D bar code, the obtained encrypted data is encoded using an appropriate channel code. The resulting 2D bar code can then be integrated directly into the digital document or can be printed onto the physical document.

The block diagram of document authentication using a 2D bar code is shown in Fig. 2. Similarly to the

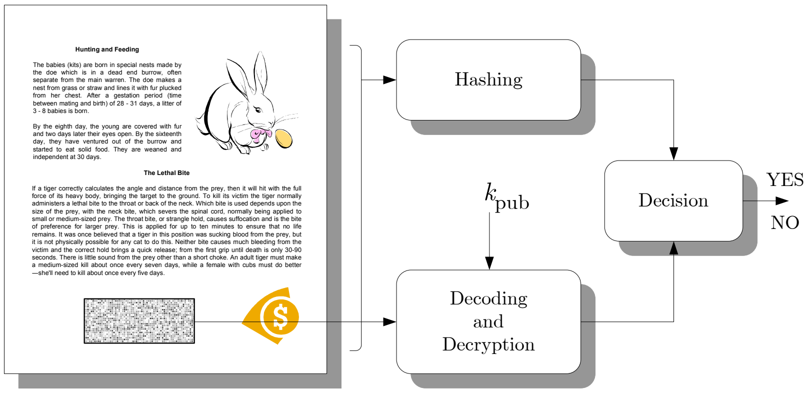

Fig. 2. Document authentication using a 2D bar code.

document enrollment procedure, the hash is computed from the entire document. Then, the hash stored into the 2D bar code is decoded and decrypted using the public key k_{pub}. Finally, the decision about the document's authenticity is made based on the comparison, in some metric space, of the obtained hashes.

Being cheap, simple and possibly exhibiting good security properties, current 2D bar codes do not offer enough storage capability for these new applications. In part, this is because most of them use only black and white (B&W) 2D symbols for representing data and corresponding binary coding technology. Examples of such 2D bar codes are Data Matrix, PDF417, Datastrip Code, QR code, etc. Only few proposals exist (commercial and non-commercial) that use *multiple gray levels* or *colors* for the 2D symbols. We call this type of symbologies *multilevel 2D bar codes*. Although multilevel 2D bar codes can potentially increase the achievable rates, in bytes per square inch (bytes/in^2), of B&W symbologies, little research has been done on how to efficiently design and implement this approach. Therefore, the main goal of this paper is to give a number of guidelines for the design of cheap and high-rate multilevel 2D bar codes.

This paper is organized as follows. The description of the problem framework and an evaluation of the performance limits of multilevel 2D bar codes is given in Section II. A new discrete model for the print-and-scan channel, specifically adapted to the problem of communications via multilevel 2D bar codes, is presented in Section III. A review of multilevel coding with multistage decoding (MLC/MSD) for the additive white Gaussian noise channel and the adaptation of this coded modulation technique to the print-and-scan channel is presented in Section IV. Experimental results on the design of practical multilevel 2D bar codes using MLC/MSD are presented in Section V. Finally, Section VI concludes the paper and describes future work.

Notations. We use small or capital letters for constants, deterministic variables, and function names. We use capital letters, e.g. X, to denote scalar random variables, bold capital letters, e.g. $\mathbf{X}$, to denote vector random variables, and corresponding small letters, e.g. x and $\mathbf{x}$, to denote their realizations. The probability mass (respectively density) function or p.m.f. (respectively p.d.f.) of a discrete (respectively continuous) random variable X is denoted by $p_X(\cdot)$ (respectively $f_X(\cdot)$). When no confusion is possible we write $p(x)$ (respectively $f(x)$) instead of $p_X(x)$ (respectively $f_X(x)$). We use $X \sim p_X(\cdot)$ to indicate that the random variable X is distributed according to $p_X(\cdot)$. The mathematical expectation of a random variable $X \sim p_X(\cdot)$ is denoted by $\mathrm{E}_{p_X}[X]$ or simply by $\mathrm{E}[X]$ or μ_X. $\mathrm{Var}[X]$ or σ_X^2 denote the variance of X. Calligraphic letters $\mathcal{X}$ denote sets and $|\mathcal{X}|$ denotes the cardinality of $\mathcal{X}$. The set of nonnegative real numbers is denoted by $\mathbb{R}^+$. The set $\{0,\ 1,\ \ldots,\ 255\}$ is denoted by [0, 255]. The entropy (respectively differential entropy) of a discrete (respectively continuous) random variable X is denoted by $\mathrm{H}(X)$

(respectively $\mathrm{h}(X)$) and the mutual information between random variables X and Y by $\mathrm{I}(X;Y)$.

II. Framework and Performance Limits of Multilevel 2D Bar Codes

The goal of this section is to evaluate the theoretical performance limits of multilevel 2D bar codes in terms of the maximum number of levels that can be placed within a 2D symbol. Here and hereafter the print-and-scan channel is studied only for the case of B&W halftone printers and low-resolution CCD-based scanners (up to 600 ppi). Therefore, all our results apply only to this specific case. However, our approach can be readily extended and applied to other print-and-scan channels, including those that use color printing and laser engraving as printing technologies.

Halftone printers simulate multiple gray levels by using the so-called halftoning technique [10]. Assume that both an ideal halftone printer and an ideal scanner are exploited in order to avoid the interference between adjacent 2D symbols. Furthermore, suppose perfect synchronization, meaning that all the 2D symbols are accurately read from their exact location on the paper. Let r_p represent the printer's resolution measured in dots per inch (dpi), a be the length in dots of the side of a square halftone cell[1] (see Fig. 3(a)), and r_s denote the scanner's resolution measured in pixels per inch (ppi). In this case, the printer produces

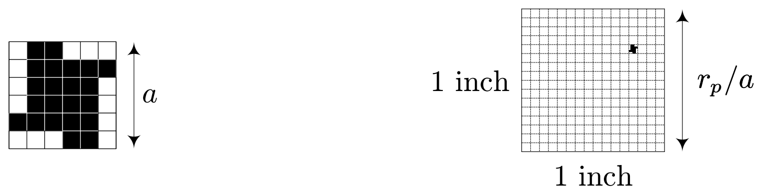

(a) (b)

Fig. 3. (a) Square halftone cell of a-by-a dots. (b) Array of halftone cells.

$(r_p/a)^2$ halftone cells per square inch (see Fig. 3(b)), each of them capable of representing up to a^2+1 gray levels [10, p. 5]. Assuming we use one halftone cell to represent one multilevel 2D symbol, we can place up to:

$$U = (r_p/a)^2 \cdot \log_2(a^2+1) \tag{1}$$

information bits per square inch.

Notice that if r_p is fixed, U is a strictly decreasing function of a (see Fig. 4). At first, this fact may appear contradictory since one expects an increase in the storage capacity of a multilevel 2D bar code

[1]The quotient r_p/a (see Fig. 3(b)) is usually known as the printer's screen frequency and is measured in lines per inch (lpi).

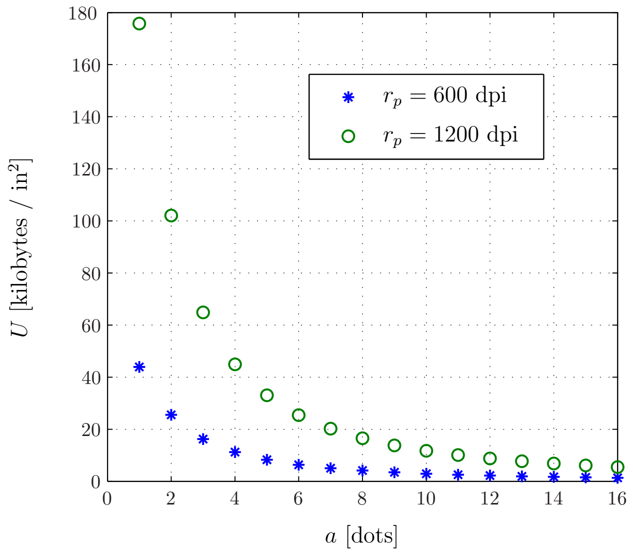

Fig. 4. Maximum number U of bits per square inch for a multilevel 2D bar code in the ideal setup.

if the number of employed gray levels is higher. However, we observe from (1) that, *due to the printing technology*, the gain in terms of storage capacity of using smaller 2D symbols is greater than the gain obtained by using multiple gray levels.

The minimum scanner resolution to read a 2D symbol in this ideal case is $r_s = r_p/a$. In practice, however, a minimum resolution of $r_s = k(r_p/a)$, with $k > 1$, is needed in order to obtain both good synchronization and mitigate the inter-symbol interference (ISI). Therefore, even if (1) is maximized for $a = 1$, which corresponds to a bi-level 2D bar code, the minimum scanner resolution r_s^{BL} required for this case may be prohibitively high. On the other hand, if $a > 1$, which corresponds to an M-level 2D bar code, with $M = a^2 + 1$, then the minimum scanner resolution r_s^{ML} required for this case is a times smaller than r_s^{BL}.

III. Discrete Print-and-Scan Channel Model for Multilevel 2D Bar Codes

We consider the problem of data transmission via the continuous print-and-scan channel[2] as a digital communications problem.

[2]Notice that the physical processes of printing and scanning are continuous. Although, strictly speaking, the actual input and output of the print-and-scan channel are digital, we assume that the granularity of the involved quantization is fine enough to let us consider the print-and-scan channel as being continuous.

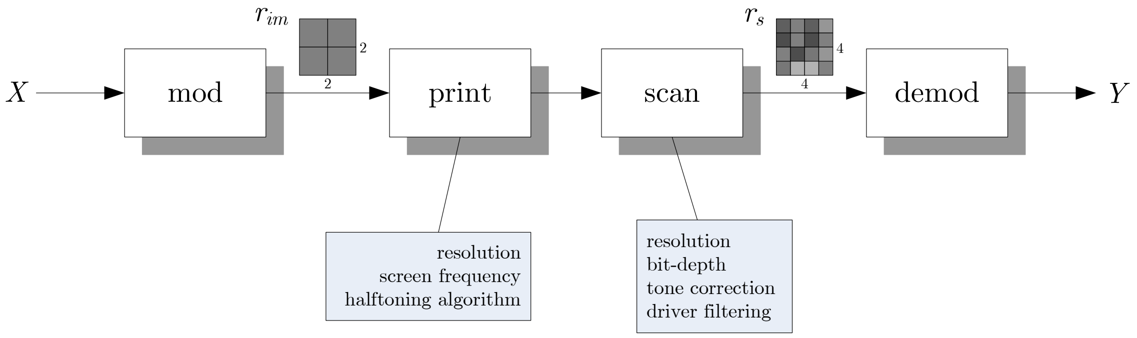

Fig. 5. Modulation and demodulation steps for communications over the print-and-scan channel.

The continuous print-and-scan channel is such that it introduces several types of distortions, specifically, luminance transformations, scaling, rotation, low pass filtering, aliasing, and noise. Furthermore, its behavior depends on the selected image resolution r_{im} (in ppi); the parameters used for printing, namely resolution r_p (in dpi), screen frequency (in lpi), and halftoning algorithm; and the parameters used for scanning, namely resolution r_s (in ppi), bit-depth, tone correction (e.g. γ-correction), and driver filtering (e.g. descreening filter).

We create multilevel 2D bar codes as digital images. Without loss of generality, we only consider the case in which $r_s \geq r_{im}$, i.e. the obtained image after printing and scanning has at least the same number of pixels as the original image[3]. Although a discrete model for the continuous print-and-scan channel has been proposed for the case where $r_s = r_{im}$ [11], [12], we do not use it here for two reasons. Firstly, because the parameters in this model are difficult to evaluate. Secondly, because we are interested in a model including the effects of both a modulator and a demodulator of multilevel 2D symbols. The discrete channel model we propose assumes that $r_s \geq r_{im}$. It models the effects of a modulator, the continuous print-and-scan channel and a demodulator. It is, however, a simplified model since it does not take into account two impairments of the continuous print-and-scan channel, namely desynchronization and interference between 2D symbols. Still, our discrete channel model shares similar properties with the one proposed in [11], [12], e.g. the dependence between the channel noise and the channel input.

A block diagram showing the different elements considered in our model is depicted in Fig. 5. Firstly, given a gray value X, the modulator creates a 2D symbol (e.g. a 2×2 pixel square) with gray value X. Then, the 2D symbol goes across the continuous print-and-scan channel. Lastly, the demodulator

[3]Notice that the printer's resolution parameter r_p determines only the *quality* of printed reproduction of gray levels whereas the image resolution parameter r_{im} determines the *size* of the printed 2D symbols.

calculates the average gray value Y of the received 2D symbol (e.g. a 4×4 pixel square if $r_s = 2 \cdot r_{im}$).

In the rest of this paper and without loss of generality, we fix the shape of a 2D symbol to be a square. Moreover, we identify a 2D symbol with a *pulse*. Therefore, the modulation technique described above is identified with pulse amplitude modulation (PAM).

A. Characterization of the Discrete Print-and-Scan Channel

In order to reveal the behavior of the discrete print-and-scan channel for multilevel 2D bar codes, a series of experiments have been performed. We exploited 5 printers and 3 scanners from various manufacturers (see Table I). All the printers were used at their highest resolution, default screen frequency,

TABLE I

PRINTERS AND SCANNERS USED FOR EXPERIMENTATION

Model	Type	Code
HP Color LaserJet 4600 (B&W mode)	laser printer	p_1
HP LaserJet 4350	laser printer	p_2
Lexmark C760 (color mode)	laser printer	p_3
OKI B63000	laser printer	p_4
HP Color DeskJet 990Cxi (color mode)	inkjet printer	p_5
Epson Perfection 3170 Photo	CCD scanner	s_1
Canon LiDE 50	CCD scanner	s_2
HP ScanJet 5300C	CCD scanner	s_3

and default halftoning algorithm. All the scanners were used at a resolution of $r_s = 600$ ppi, in grayscale mode, and bit-depth set to 8 bits. All the other scanning parameters were set to their default values, however, automatic tone correction and filtering were switched off.

Furthermore, we used 2×2 pixel square 2D symbols and 1 pixel of inter-symbol space in order to avoid ISI. The image resolution parameter of all our digital images was set to $r_{im} = 200$ ppi. In the scope of this work we did not consider any synchronization algorithm. However, in order to deal with rotation and scaling, two typical impairments of the continuous print-and-scan channel, we manually rotated the scanned images and subsequently performed a bicubic interpolation so as to obtain the desired size for these images. As an example, we show in Fig. 6 the original and noisy versions of a multilevel 2D bar code (laser) printed-and-scanned under the above conditions.

For the characterization of the discrete print-and-scan channel, all the gray levels from 0 (black) to 255 (white) were used. For each gray level $x \in [0, 255]$, $J = 1024$ 2D symbols with gray level x were

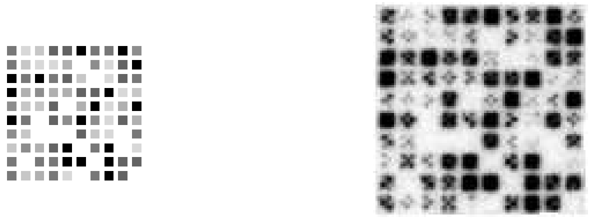

(a) (b)

Fig. 6. Multilevel 2D bar code. (a) Original digital image: 2×2 pixel symbols, 1 pixel of inter-symbol space, $r_{im} = 200$ ppi. (b) Printed-and-scanned digital image: $r_p = 600$ dpi, $r_s = 600$ ppi, 6×6 pixel noisy symbols.

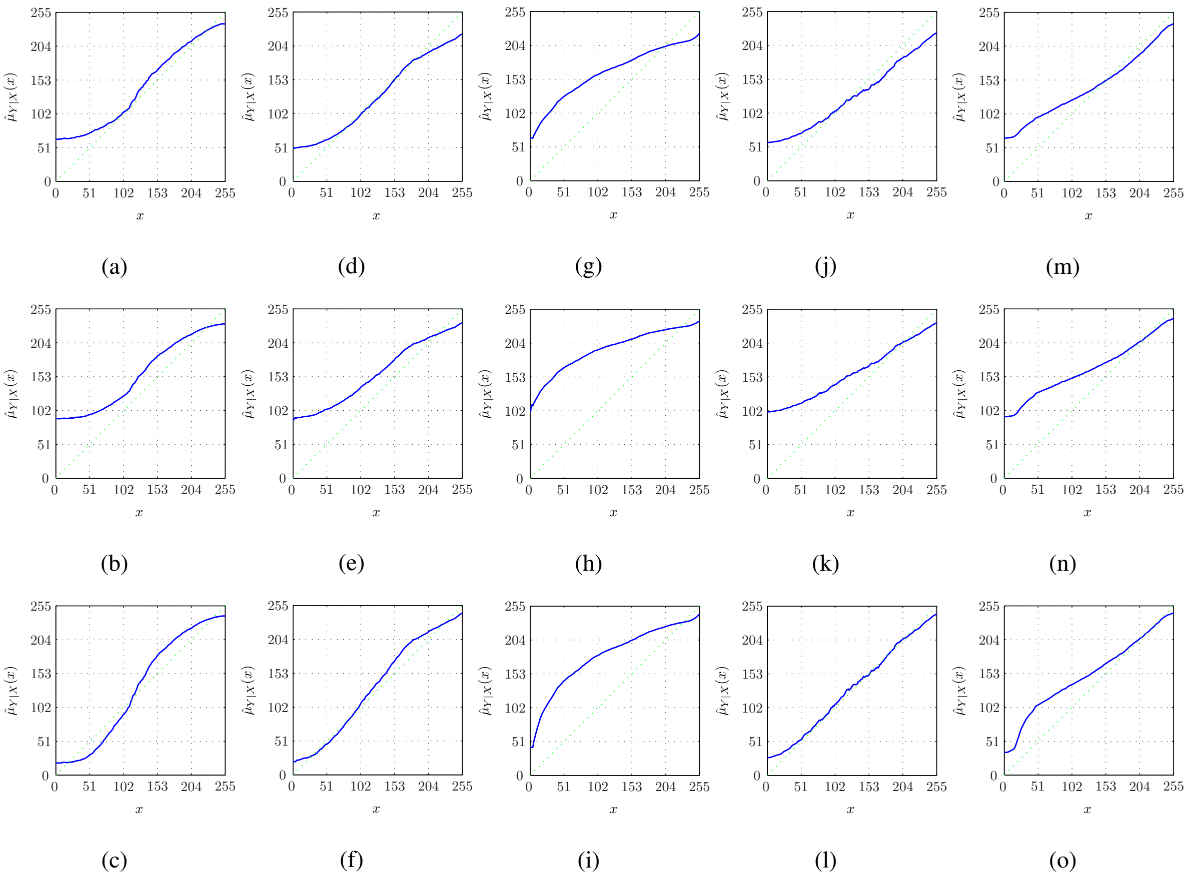

Fig. 7. Sample mean $\hat{\mu}_{Y|X}(x)$ for different combinations of printers and scanners (see Table I): (a) $p_1 - s_1$ (b) $p_1 - s_2$ (c) $p_1 - s_3$ (d) $p_2 - s_1$ (e) $p_2 - s_2$ (f) $p_2 - s_3$ (g) $p_3 - s_1$ (h) $p_3 - s_2$ (i) $p_3 - s_3$ (j) $p_4 - s_1$ (k) $p_4 - s_2$ (l) $p_4 - s_3$ (m) $p_5 - s_1$ (n) $p_5 - s_2$ (o) $p_5 - s_3$.

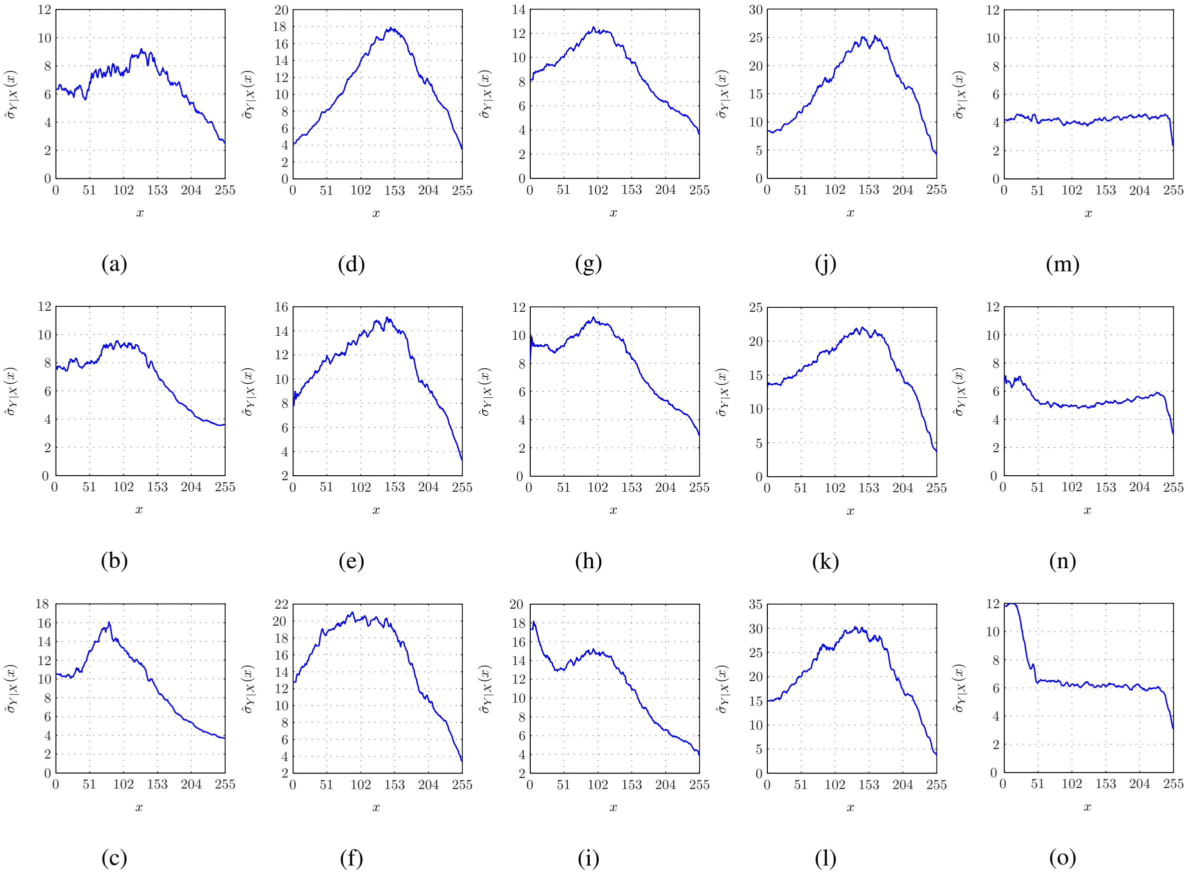

Fig. 8. Sample standard deviation $\hat{\sigma}_{Y|X}(x)$ for different combinations of printers and scanners (see Table I): (a) $p_1 - s_1$ (b) $p_1 - s_2$ (c) $p_1 - s_3$ (d) $p_2 - s_1$ (e) $p_2 - s_2$ (f) $p_2 - s_3$ (g) $p_3 - s_1$ (h) $p_3 - s_2$ (i) $p_3 - s_3$ (j) $p_4 - s_1$ (k) $p_4 - s_2$ (l) $p_4 - s_3$ (m) $p_5 - s_1$ (n) $p_5 - s_2$ (o) $p_5 - s_3$.

sent over the continuous print-and-scan channel. Then, the sample mean $\hat{\mu}_{Y|X}(x)$ and sample variance $\hat{\sigma}^2_{Y|X}(x)$ of the received noisy symbols $y_j(x) \in \mathbb{R}$, $j = 1, \ldots, J$, were computed[4]. The demodulation algorithm (see Fig. 5) that was used consisted in averaging the gray values of all but the borderline pixels of a noisy 2D symbol. We did not take into account the borderline pixels in order to reduce desynchronization problems and to avoid ISI. The choice $r_s = 600$ ppi is also justified by the same reasons.

We show in Figures 7 and 8 the obtained results for each printer and scanner combination of Table I.

[4]The following estimators were used: $\hat{\mu}_{Y|X}(x) = \frac{1}{J}\sum_{j=1}^{J} y_j(x)$ and $\hat{\sigma}^2_{Y|X}(x) = \frac{1}{J}\sum_{j=1}^{J}(y_j(x) - \hat{\mu}_{Y|X}(x))^2$.

B. *Characterization of the Noise Probability Distribution*

In this section, we study the problem of characterization of the noise probability distribution. We consider signal constellations composed of eight gray levels (see Table II). The procedure used to select these signal constellations is explained in Sect. V-A.

TABLE II

TESTED SIGNAL CONSTELLATIONS FOR CHARACTERIZING THE NOISE PROBABILITY DISTRIBUTION

	$\mathcal{X}$
$p_1 - s_1$	$\{0, 87, 116, 138, 166, 196, 224, 255\}$
$p_1 - s_2$	$\{0, 88, 118, 138, 161, 187, 213, 255\}$
$p_1 - s_3$	$\{0, 80, 113, 134, 155, 182, 211, 255\}$
$p_2 - s_1$	$\{0, 54, 88, 119, 153, 190, 231, 255\}$
$p_2 - s_2$	$\{0, 59, 96, 131, 161, 199, 234, 255\}$
$p_2 - s_3$	$\{0, 59, 95, 129, 160, 197, 234, 255\}$
$p_3 - s_1$	$\{0, 15, 35, 65, 113, 174, 230, 255\}$
$p_3 - s_2$	$\{0, 10, 27, 50, 94, 161, 225, 255\}$
$p_3 - s_3$	$\{0, 14, 33, 62, 110, 174, 231, 255\}$
$p_4 - s_1$	$\{0, 54, 93, 136, 181, 218, 241, 255\}$
$p_4 - s_2$	$\{0, 63, 105, 154, 190, 222, 243, 255\}$
$p_4 - s_3$	$\{0, 52, 90, 131, 181, 217, 241, 255\}$
$p_5 - s_1$	$\{0, 45, 94, 137, 173, 204, 230, 255\}$
$p_5 - s_2$	$\{0, 36, 76, 123, 164, 197, 227, 255\}$
$p_5 - s_3$	$\{0, 31, 67, 114, 156, 193, 225, 255\}$

We assigned uniform a-priori probabilities to the signal constellation points and sent the corresponding 2D bar code symbols $J = 8192$ times over the continuous print-and-scan channel. We show in Fig. 9 the normalized histograms of the *received* signal points for all printer and scanner combinations. We observe from this figure that given a signal point $x \in \mathcal{X}$, the conditional probability distribution $f_{Y|X}(\cdot|x)$ of $(Y|X = x)$ may be modeled, as first approximation, by a *generalized Gaussian distribution* (GGD) [13] with mean $\hat{\mu}_{Y|X}(x)$, standard deviation $\hat{\sigma}_{Y|X}(x)$, and shape factor $\hat{\gamma}_{Y|X}(x)$, i.e. $(Y|X = x) \sim \mathcal{GGD}(\hat{\mu}_{Y|X}(x), \hat{\sigma}_{Y|X}(x), \hat{\gamma}_{Y|X}(x))$ [5]. The corresponding estimated parameters are shown in Table III.

As we will see in Section V, the main justification of the proposed model is that it gives reasonably good results for the problem of data transmission over the continuous print-and-scan channel via multilevel

[5]Recall that if $X \sim \mathcal{GGD}(\mu, \sigma, \gamma)$, then the p.d.f. of X is given by:

$$f_X(x) = \frac{\gamma\eta(\sigma,\gamma)}{2\Gamma(1/\gamma)} \exp\left(-[\eta(\sigma,\gamma)|x-\mu|]^{\gamma}\right),$$

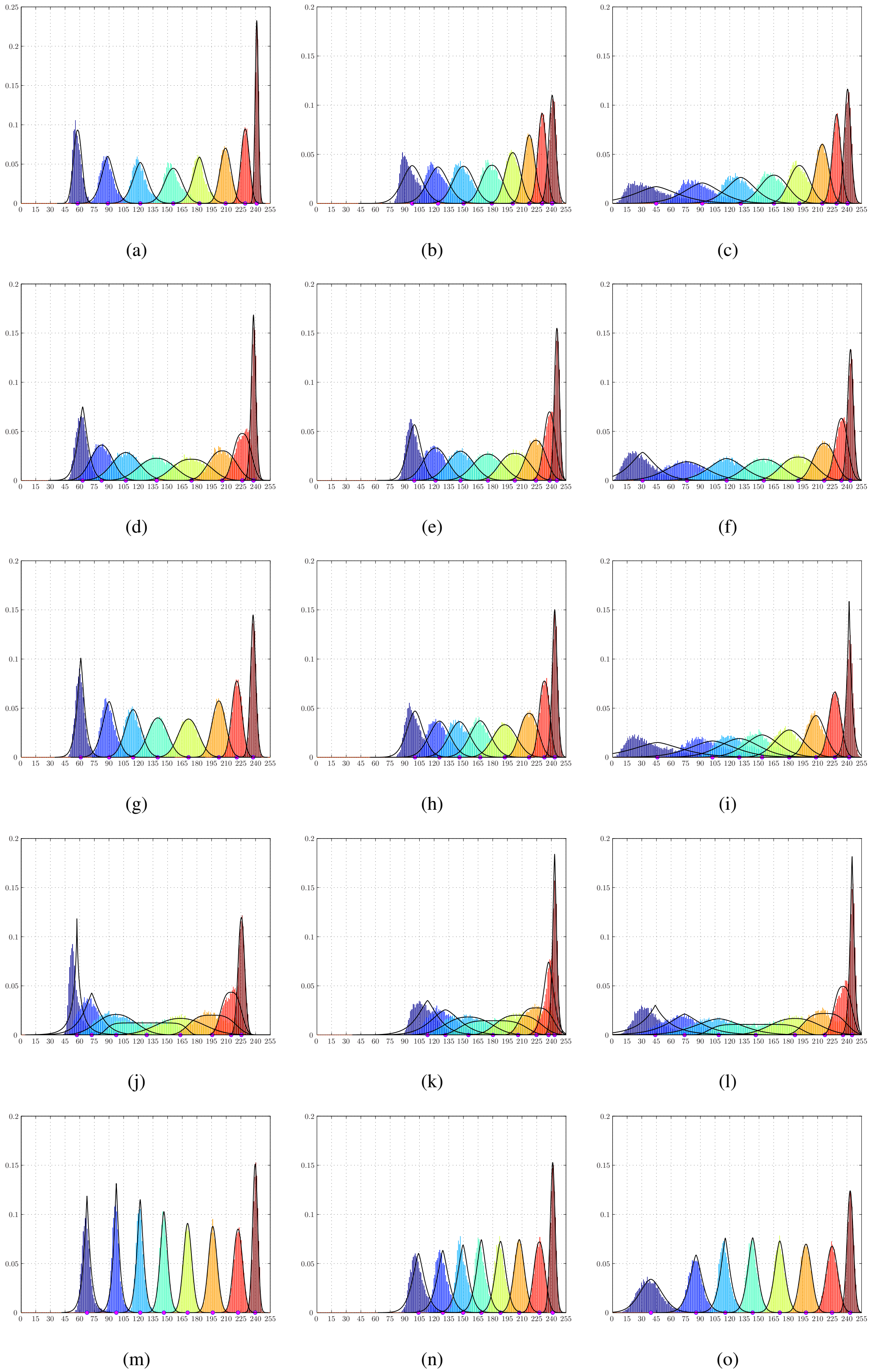

(a) (b) (c) (d) (e) (f) (g) (h) (i) (j) (k) (l) (m) (n) (o)

Fig. 9. Normalized histogram of the received signal points and GGD approximation for each $x \in \mathcal{X}$ (see Tables II and III): (a) $p_1 - s_1$ (b) $p_1 - s_2$ (c) $p_1 - s_3$ (d) $p_2 - s_1$ (e) $p_2 - s_2$ (f) $p_2 - s_3$ (g) $p_3 - s_1$ (h) $p_3 - s_2$ (i) $p_3 - s_3$ (j) $p_4 - s_1$ (k) $p_4 - s_2$ (l) $p_4 - s_3$ (m) $p_5 - s_1$ (n) $p_5 - s_2$ (o) $p_5 - s_3$.

TABLE III

ESTIMATED PARAMETERS FOR THE GGD APPROXIMATION OF THE NOISE PROBABILITY DISTRIBUTION: (a) $p_1 - s_1$ (b) $p_1 - s_2$ (c) $p_1 - s_3$ (d) $p_2 - s_1$ (e) $p_2 - s_2$ (f) $p_2 - s_3$ (g) $p_3 - s_1$ (h) $p_3 - s_2$ (i) $p_3 - s_3$ (j) $p_4 - s_1$ (k) $p_4 - s_2$ (l) $p_4 - s_3$ (m) $p_5 - s_1$ (n) $p_5 - s_2$ (o) $p_5 - s_3$.

(a)

x	$\hat{\mu}_{Y\|X}(x)$	$\hat{\sigma}_{Y\|X}(x)$	$\hat{\gamma}_{Y\|X}(x)$
0	57.9	4.20	2.07
87	88.7	7.48	1.64
116	122.1	8.43	1.68
138	155.8	8.98	1.98
166	182.6	7.62	1.63
196	209.3	5.69	2.00
224	229.4	4.15	2.06
255	241.3	1.75	1.92

(b)

x	$\hat{\mu}_{Y\|X}(x)$	$\hat{\sigma}_{Y\|X}(x)$	$\hat{\gamma}_{Y\|X}(x)$
0	97.56	11.01	1.79
88	123.96	11.40	1.79
118	150.12	10.45	2.04
138	179.13	9.62	2.31
161	200.57	7.51	2.12
187	217.50	5.75	1.99
213	230.55	4.39	1.97
255	240.88	3.80	1.83

(c)

x	$\hat{\mu}_{Y\|X}(x)$	$\hat{\sigma}_{Y\|X}(x)$	$\hat{\gamma}_{Y\|X}(x)$
0	44.75	27.73	1.51
80	91.88	21.52	1.63
113	131.43	16.50	1.70
134	165.34	13.60	2.08
155	191.31	10.11	2.09
182	214.77	6.55	2.05
211	229.49	4.51	1.90
255	240.69	3.59	1.84

(d)

x	$\hat{\mu}_{Y\|X}(x)$	$\hat{\sigma}_{Y\|X}(x)$	$\hat{\gamma}_{Y\|X}(x)$
0	63.04	6.83	1.37
54	82.47	10.96	2.04
88	107.16	14.07	1.99
119	138.80	16.67	2.28
153	174.57	16.71	2.53
190	206.01	12.16	2.43
231	226.48	7.51	2.58
255	237.91	2.64	1.65

(e)

x	$\hat{\mu}_{Y\|X}(x)$	$\hat{\sigma}_{Y\|X}(x)$	$\hat{\gamma}_{Y\|X}(x)$
0	99.71	7.58	1.74
59	121.48	11.76	2.11
96	147.03	13.48	1.97
131	175.14	14.44	2.13
161	202.70	13.10	2.56
199	224.23	9.18	2.30
234	238.23	5.55	2.13
255	245.71	2.57	2.00

(f)

x	$\hat{\mu}_{Y\|X}(x)$	$\hat{\sigma}_{Y\|X}(x)$	$\hat{\gamma}_{Y\|X}(x)$
0	30.81	17.50	1.40
59	76.32	21.95	1.83
95	116.86	19.06	1.78
129	154.89	17.60	2.26
160	190.18	15.42	2.42
197	216.80	9.92	2.30
234	234.38	6.11	2.14
255	243.66	3.14	1.83

(g)

x	$\hat{\mu}_{Y\|X}(x)$	$\hat{\sigma}_{Y\|X}(x)$	$\hat{\gamma}_{Y\|X}(x)$
0	61.10	5.36	1.28
15	90.13	7.85	1.65
35	114.74	8.48	1.89
65	139.92	9.79	2.07
113	171.47	10.03	2.09
174	202.47	6.86	2.06
230	220.85	5.05	2.07
255	237.52	2.96	1.75

(h)

x	$\hat{\mu}_{Y\|X}(x)$	$\hat{\sigma}_{Y\|X}(x)$	$\hat{\gamma}_{Y\|X}(x)$
0	100.42	9.17	1.73
10	125.50	11.23	1.87
27	146.04	11.42	1.86
50	167.22	11.19	1.85
94	192.39	11.76	2.10
161	217.23	8.23	2.41
225	232.94	4.83	2.29
255	243.47	2.88	1.73

(i)

x	$\hat{\mu}_{Y\|X}(x)$	$\hat{\sigma}_{Y\|X}(x)$	$\hat{\gamma}_{Y\|X}(x)$
0	45.96	31.89	1.48
14	102.30	26.85	1.65
33	129.80	22.19	1.79
62	153.18	18.90	1.74
110	180.97	14.63	1.93
174	208.42	9.54	1.94
231	227.67	5.93	2.06
255	242.28	3.92	1.11

(j)

x	$\hat{\mu}_{Y\|X}(x)$	$\hat{\sigma}_{Y\|X}(x)$	$\hat{\gamma}_{Y\|X}(x)$
0	57.16	10.28	0.69
54	72.30	13.65	1.19
93	97.37	18.17	2.24
136	128.60	24.16	9.12
181	163.04	22.86	2.16
218	195.65	16.55	3.35
241	215.03	7.93	2.92
255	225.53	3.28	2.07

(k)

x	$\hat{\mu}_{Y\|X}(x)$	$\hat{\sigma}_{Y\|X}(x)$	$\hat{\gamma}_{Y\|X}(x)$
0	113.27	15.41	1.29
63	131.62	18.20	1.55
105	155.15	20.07	2.42
154	180.24	22.03	4.12
190	205.98	17.25	2.88
222	224.82	12.00	3.45
243	237.21	6.05	1.63
255	243.38	2.68	1.43

(l)

x	$\hat{\mu}_{Y\|X}(x)$	$\hat{\sigma}_{Y\|X}(x)$	$\hat{\gamma}_{Y\|X}(x)$
0	43.83	23.93	0.98
52	73.79	25.07	1.30
90	108.77	26.61	1.70
131	146.64	28.12	6.64
181	186.83	22.37	2.29
217	217.46	15.32	3.26
241	235.97	7.13	2.73
255	245.30	2.88	1.33

(m)

x	$\hat{\mu}_{Y\|X}(x)$	$\hat{\sigma}_{Y\|X}(x)$	$\hat{\gamma}_{Y\|X}(x)$
0	67.5	5.24	1.12
45	97.5	4.40	1.20
94	121.9	4.27	1.44
137	146.2	4.35	1.64
173	170.5	4.57	1.86
204	196.2	4.69	1.88
230	222.1	4.64	2.05
255	239.6	2.68	1.95

(n)

x	$\hat{\mu}_{Y\|X}(x)$	$\hat{\sigma}_{Y\|X}(x)$	$\hat{\gamma}_{Y\|X}(x)$
0	104.06	8.39	1.39
36	128.89	7.89	1.41
76	149.63	6.96	1.48
123	168.35	6.47	1.48
164	188.03	6.17	1.63
197	207.22	5.71	1.78
227	227.78	5.36	2.14
255	241.43	2.76	1.80

(o)

x	$\hat{\mu}_{Y\|X}(x)$	$\hat{\sigma}_{Y\|X}(x)$	$\hat{\gamma}_{Y\|X}(x)$
0	39.29	12.73	1.73
31	85.55	8.24	1.47
67	115.48	6.76	1.36
114	143.53	6.05	1.57
156	171.28	6.01	1.69
193	198.10	5.81	1.94
225	224.77	5.89	2.01
255	243.34	3.23	1.99

2D bar codes.

C. Print-and-Scan Discrete Channel Model

Based on our experimental results, reported in Sections III-A and III-B, we model the print-and-scan channel as (see also Fig. 10):

$$Y = \varphi(X) + Z, \quad X \in \mathcal{X} = [0, 255], \quad Y \in \mathcal{Y} = \mathbb{R}, \tag{2}$$

where X (the channel input) represents the gray value of a 2D symbol, $\varphi : \mathcal{X} \to \mathbb{R}$ is a nonlinear function representing the response of the print-and-scan channel, Z represents zero-mean additive noise, and Y (the channel output) represents the obtained gray value of the corresponding 2D symbol. Gray values are represented as numbers in the set $\{0, 1, \ldots, 255\}$. The function $\varphi(\cdot)$ is in general different for

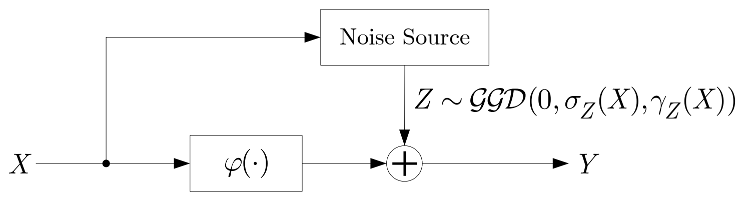

Fig. 10. Discrete model for the print-and-scan channel.

every particular instance of the print-and-scan channel, i.e. for every printer and scanner combination. Contrary to what is usually assumed, the noise term Z is not supposed to be independent of the gray value X. This is in agreement with the discrete model proposed in [11], [12]. In fact, according to the experimental results reported in Sect. III-B, we suppose that for each channel use Z is drawn i.i.d. from a zero-mean *generalized Gaussian distribution* with standard deviation and shape factor depending on the channel input X. Thus, we model $(Z|X = x)$ as:

$$(Z|X = x) \sim \mathcal{GGD}(0, \sigma_Z(x), \gamma_Z(x)) \tag{3}$$

where, $\sigma_Z(x)$ and $\gamma_Z(x)$ are, respectively, the noise standard deviation and shape factor given that $X = x$. As a final remark, notice that our discrete channel model assumes perfect synchronization and absence of ISI.

where μ, σ, and γ denote, respectively, the *mean*, the *standard deviation*, and the *shape factor* of X, $\Gamma(\cdot)$ denotes the gamma function, and:

$$\eta(\sigma, \gamma) = \frac{1}{\sigma}\sqrt{\frac{\Gamma(3/\gamma)}{\Gamma(1/\gamma)}}.$$

For practical schemes based on this model, the channel response $\varphi(\cdot)$ is approximated by the sample mean $\hat{\mu}_{Y|X}(\cdot)$, i.e. $\varphi(x) = \hat{\mu}_{Y|X}(x)$, the noise standard deviation $\sigma_Z(\cdot)$ by the sample standard deviation $\hat{\sigma}_{Y|X}(\cdot)$, i.e. $\sigma_Z(x) = \hat{\sigma}_{Y|X}(x)$, and the noise shape factor $\gamma_Z(\cdot)$ by the sample shape factor $\hat{\gamma}_{Y|X}(\cdot)$, i.e. $\gamma_Z(x) = \hat{\gamma}_{Y|X}(x)$.

IV. Multilevel Coding for the Discrete Print-and-Scan Channel

In Sect. III-C, we modeled the print-and-scan channel as a (discrete) channel with luminance-dependent generalized Gaussian additive noise. Moreover, we showed in Sect. III-B that the estimated noise shape factors are, in most cases, close to 2. In this section, inspired by the results obtained in [14] for the AWGN channel, we study the suitability of multilevel coding together with multistage decoding (MLC/MSD) for the print-and-scan channel. Thus, the goal of this section is twofold. Firstly, we consider the fundamentals of MLC/MSD for the discrete AWGN channel. Secondly, we adapt the theory of multilevel coding to the case of the discrete print-and-scan channel modeled by (2) and (3).

A. *Multilevel Coding for the AWGN Channel*

The idea of coded modulation is to jointly optimize coding and modulation in order to improve the performance of digital communication schemes [15]. MLC/MSD is a well-known bandwidth-efficient scheme for the AWGN channel in the high-SNR regime [16]. In the following paragraphs we recall the fundamental results concerning MLC/MSD.

Consider the discrete AWGN channel model:

$$Y = X + Z, \quad X \in \mathcal{X}, \quad Y \in \mathcal{Y}, \quad Z \sim \mathcal{N}(0, \sigma_Z^2),$$

where X (respectively Y) is the channel input (respectively output), $\mathcal{X}$ (respectively $\mathcal{Y}$) is the input (respectively output) alphabet, and Z represents the noise. For each channel use, the noise Z is drawn i.i.d. from a zero-mean Gaussian distribution with variance σ_Z^2 and is assumed to be independent from the channel input X. This model can be considered as a particular case of model (2) and (3) under the assumption that $\varphi(x) = x$, $\sigma_Z(x) = \sigma_Z$, and $\gamma_Z(x) = 2$, for all $x \in \mathcal{X}$. Given the channel input variance σ_X^2, the capacity of this channel, in bits per channel use, is:

$$C_{\text{AWGN}} = \max_{f_X(\cdot)} \mathrm{I}(X;Y) = \frac{1}{2}\log_2\left(1 + \frac{\sigma_X^2}{\sigma_Z^2}\right),$$

which is attained when the channel input X is Gaussian, for example $X \sim \mathcal{N}(\mu_X, \sigma_X^2)$.

Due to the technical impossibility of using either a continuous or an infinite input alphabet, practical systems usually employ a discrete and finite $M = 2^L-$ary input alphabet (signal constellation), i.e.

$|\mathcal{X}| = 2^L$. For example, we show in Fig. 11 a PAM signal constellation with $M = 8$ ($L = 3$) equidistant signal points.

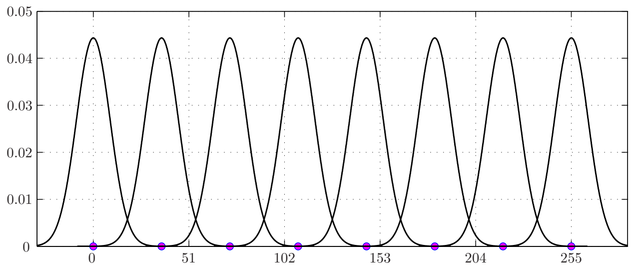

Fig. 11. Transmission of an 8–PAM equidistant constellation over the AWGN channel.

It is customary to assign a binary label to each signal point by means of a bijective mapping ψ:

$$(b^0, b^1, \ldots, b^{L-1}) \underset{\psi}{\mapsto} x, \tag{4}$$
$$b^i \in \mathcal{B} = \{0, 1\}, \quad x \in \mathcal{X}, \quad i = 0, 1, \ldots, L-1.$$

Given a specific probability distribution $\{p(x) : x \in \mathcal{X}\}$ over the channel inputs, the maximum rate of reliable communications of such systems is given by the mutual information $\mathrm{I}(X;Y)$.

Remarkably, MLC/MSD [14], [17], [18] is a straightforward consequence of the chain rule for mutual information. Since the mapping ψ in (4) is bijective, the mutual information $\mathrm{I}(X;Y)$ between the transmitted signal X and the received signal Y equals the mutual information $\mathrm{I}(B^0, B^1, \ldots, B^{L-1}; Y)$ between the binary label of X and the received signal Y. Applying the chain rule for mutual information, we get:

$$\begin{aligned} \mathrm{I}(X;Y) &= \mathrm{I}(B^0, B^1, \ldots, B^{L-1}; Y) \\ &= \mathrm{I}(B^0;Y) + \mathrm{I}(B^1;Y|B^0) + \ldots + \mathrm{I}(B^{L-1};Y|B^0, B^1, \ldots, B^{L-2}). \end{aligned} \tag{5}$$

Equation (5) can be interpreted as follows. Transmission of vectors with binary digits $b^i, i = 0, 1, \ldots, L-1$, over the physical channel can be separated into the parallel transmission of individual bits b^i over L equivalent channels, provided that $b^0, b^1, \ldots, b^{i-1}$ are known (see Figs. 12 and 13).

At the transmitter side (see Fig. 14), a binary data block of length K bits is partitioned into L sub-

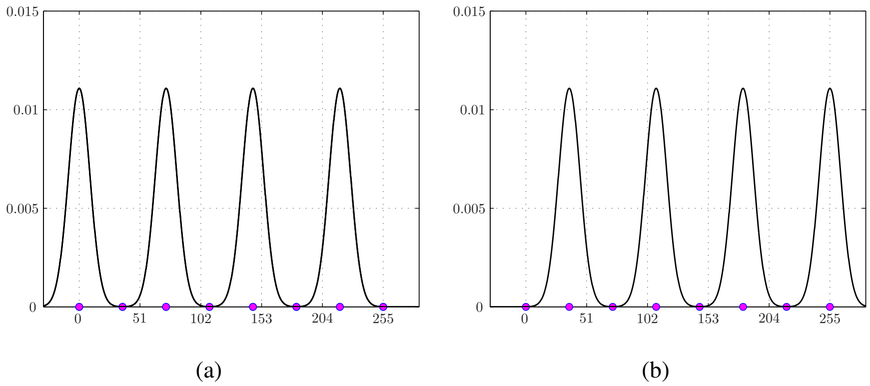

Fig. 12. Conditional p.d.f.'s for the equivalent channel at level 0 when an 8–PAM equidistant constellation with Ungerböck's labeling is used: (a) $f(y|b^0 = 0)$, (b) $f(y|b^0 = 1)$.

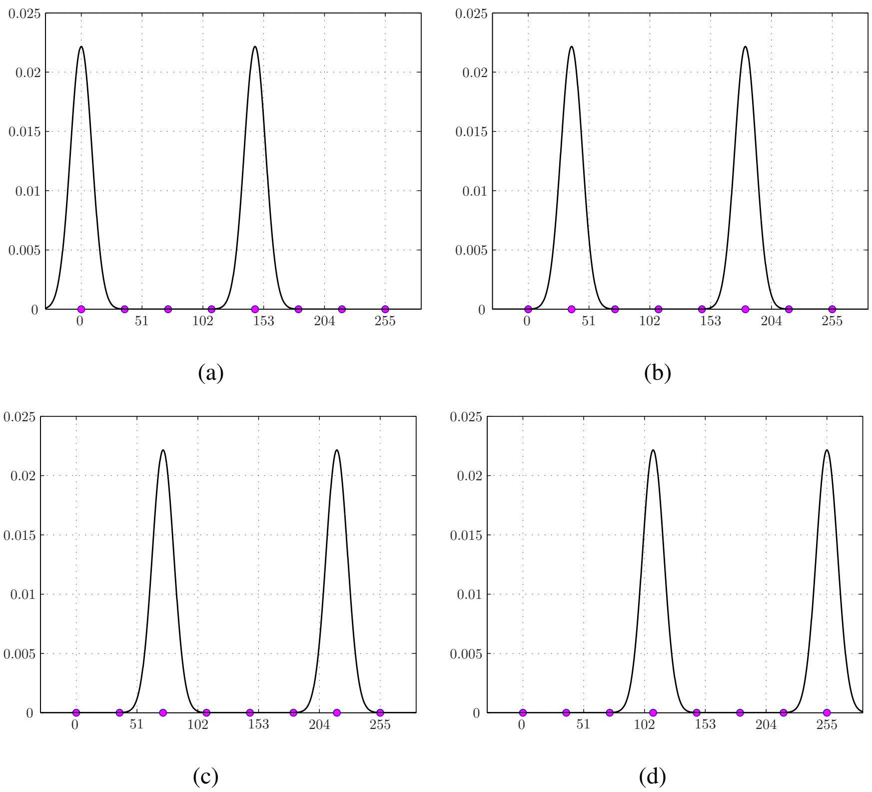

Fig. 13. Conditional p.d.f.'s for the equivalent channel at level 1 when an 8–PAM equidistant constellation with Ungerböck's labeling is used: (a) $f(y|b^1 = 0, b^0 = 0)$, (b) $f(y|b^1 = 0, b^0 = 1)$, (c) $f(y|b^1 = 1, b^0 = 0)$, (d) $f(y|b^1 = 1, b^0 = 1)$.

blocks:

$$\mathbf{q} = (q_1, \dots, q_K), \quad q_k \in \mathcal{B}, \quad k = 1, \dots, K,$$
$$\mathbf{q} = (\mathbf{q}^0, \dots, \mathbf{q}^{L-1}), \quad \mathbf{q}^i = (q_1^i, \dots, q_{K_i}^i),$$
$$i = 0, 1, \dots, L-1, \quad \sum_{i=0}^{L-1} K_i = K.$$

Each data sub-block $\mathbf{q}^i$ is fed into an individual binary encoder E_i of rate $R_i = K_i/N$ producing a codeword:

$$\mathbf{b}^i = (b_1^i, \dots, b_N^i), \quad b_n^i \in \mathcal{B},$$
$$n = 1, \dots, N, \quad i = 0, 1, \dots, L-1,$$

of the corresponding component code. In this manner L levels of coding are created. For simplicity,

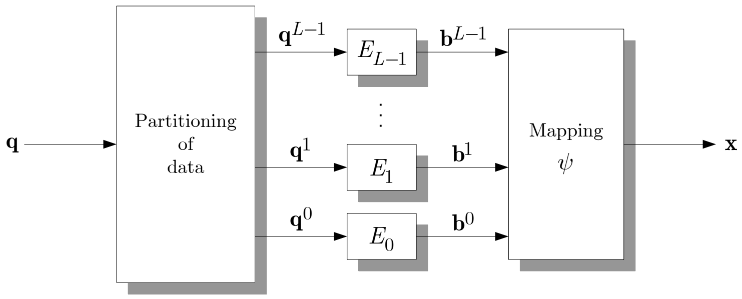

Fig. 14. Multilevel encoder.

we assume that all codewords have equal length, N binary symbols, at all levels. Then, the n-th bit b_n^i, $n = 1, \dots, N$, of every codeword $\mathbf{b}^i$ is selected to form a binary label $(b_n^0, b_n^1, \dots, b_n^{L-1})$ of L bits, which is mapped via ψ to a signal point $x_n \in \mathcal{X}$. In this way, we obtain a vector:

$$\mathbf{x} = (x_1, \dots, x_N), \quad x_n \in \mathcal{X}, \quad n = 1, \dots, N,$$

of N channel inputs, which are serially transmitted over the AWGN channel. It is very easy to show that the code rate of the overall scheme, $R = K/N$, is equal to the sum of the individual code rates:

$$\sum_{i=0}^{L-1} R_i = \sum_{i=0}^{L-1} \frac{K_i}{N} = \frac{1}{N} \sum_{i=0}^{L-1} K_i = \frac{K}{N} = R.$$

At the receiver side, the component codes are successively decoded by the corresponding decoders starting from the lowest level. At any stage i, $i = 0, 1, \dots, L-1$, the decoder processes not only the N

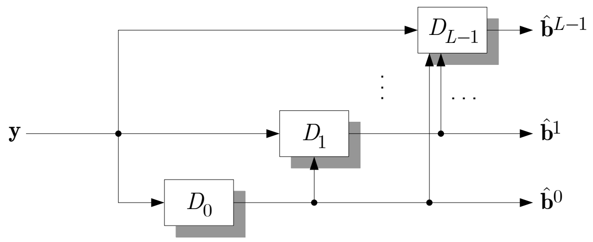

Fig. 15. Multistage decoder.

received signal points:

$$\mathbf{y} = (y_1, \ldots, y_N), \quad y_n \in \mathcal{Y}, \quad n = 1, \ldots, N,$$

but also decisions of previous decoding stages:

$$\hat{\mathbf{b}}^j = (\hat{b}_1^j, \ldots, \hat{b}_N^j), \quad \hat{b}_n^j \in \mathcal{B},$$

$$n = 1, \ldots, N, \quad j = 0, 1, \ldots, i-1.$$

The block diagram of the receiver is shown in Fig. 15. For simplicity, this diagram represents neither the “Data selection” block, which outputs $\hat{\mathbf{q}}^0, \ldots, \hat{\mathbf{q}}^{L-1}$, nor the “Concatenation of data” block, which outputs $\hat{\mathbf{q}}$.

One can demonstrate that the maximum achievable rate of a modulation scheme (e.g. 8–PAM) with given a-priori probabilities of its signal constellation points can indeed be achieved by MLC/MSD if, and only if, the individual rates R_i of the component codes are chosen to be equal to the capacities of the equivalent channels, i.e:

$$R_i = \mathrm{I}(B^i; Y | B^0, B^1, \ldots, B^{i-1}), \quad i = 0, 1, \ldots, L-1.$$

This is the so-called *capacity rule* for choosing the individual code rates [14] (see Fig. 16).

The capacity rule does not indicate however which codes to use for the equivalent channels. In practice, since the statistics of the equivalent channels $f(y|b^i, b^0, ..., b^{i-1})$ are highly non Gaussian (see Figs. 12 and 13) and no optimal codes are known for these channels, one has some freedom for selecting the individual codes. In previous work, it was shown that very long Turbo codes and low density parity-check (LDPC) codes perform very well on MLC/MSD schemes for the AWGN channel [19], [20].

Moreover, since the capacity rule applies to any labeling, there is no restriction on the particular labeling used in MLC/MSD. Nevertheless, for finite codeword length, Ungerböck’s labeling turns out to show the highest performance among MLC/MSD schemes with different labelings [14].

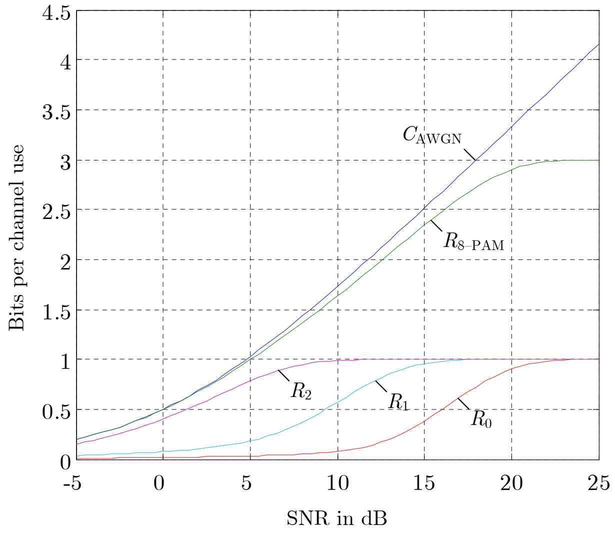

Fig. 16. Capacity rule for selecting the individual code rates.

It should also be mentioned that MLC/MSD is not the only capacity-approaching coded modulation technique for the AWGN channel. The interested reader can find details about some other techniques in [21]–[25].

B. Multilevel Coding for the Print-and-Scan Channel

Suppose we use an M–ary ($|\mathcal{X}| = M = 2^L$) modulation system with given a-priori probabilities of the signal constellation points $\{p(x) : x \in \mathcal{X}\}$. Since our channel is memoryless, i.e. the output Y depends solely on the current channel input X and current noise term Z, the maximum achievable rate of this modulation system is given by the mutual information $\mathrm{I}(X;Y)$. Although we cannot provide a closed-form expression for $\mathrm{I}(X;Y)$ it is fairly easy to compute it numerically. By definition:

$$\mathrm{I}(X;Y) = \mathrm{h}(Y) - \mathrm{h}(Y|X). \tag{6}$$

Firstly, we can compute the term $\mathrm{h}(Y)$ in (6) as follows. By definition:

$$\mathrm{h}(Y) = -\int_{\mathcal{Y}} f(y) \log f(y)\, \mathrm{d}y. \tag{7}$$

In order to numerically evaluate the integral in (7), we need to specify $f(y)$. This can be done by conditioning on $X = x$:

$$f(y) = \sum_{x \in \mathcal{X}} f(y|x) p(x). \tag{8}$$

The term $f(y|x)$ in (8) can be obtained noting that $(Y|X=x)$ has a generalized Gaussian distribution with mean $\varphi(x)$, standard deviation $\sigma_Z(x)$, and shape factor $\gamma_Z(x)$, i.e. $(Y|X=x) \sim \mathcal{GGD}(\varphi(x), \sigma_Z(x), \gamma_Z(x))$.

Secondly, the term $\mathrm{h}(Y|X)$ in (6) can be computed as follows:

$$\mathrm{h}(Y|X) = \mathrm{h}(\varphi(X) + Z|X) = \mathrm{h}(Z|X) = \sum_{x \in \mathcal{X}} \mathrm{h}(Z|X=x)p(x),$$

where we used (2) and the definition of conditional differential entropy [26]. Since $(Z|X=x)$ has a generalized Gaussian distribution with zero mean, standard deviation $\sigma_Z(x)$, and shape factor $\gamma_Z(x)$, we have:

$$\mathrm{h}(Z|X=x) = \log_2\left(\frac{2\cdot\Gamma(1/\gamma_Z(x))\exp(1/\gamma_Z(x))}{\gamma_Z(x)\eta(\sigma_Z(x),\gamma_Z(x))}\right).$$

Therefore,

$$\begin{aligned}\mathrm{h}(Y|X) &= \sum_{x\in\mathcal{X}} \log_2\left(\frac{2\cdot\Gamma(1/\gamma_Z(x))\exp(1/\gamma_Z(x))}{\gamma_Z(x)\eta(\sigma_Z(x),\gamma_Z(x))}\right)p(x)\\ &= \mathrm{E}_{p_X}\left[\log_2\left(\frac{2\cdot\Gamma(1/\gamma_Z(X))\exp(1/\gamma_Z(X))}{\gamma_Z(X)\eta(\sigma_Z(X),\gamma_Z(X))}\right)\right].\end{aligned}$$

Although we are able to compute $\mathrm{I}(X;Y)$ for any given input distribution $p_X(\cdot)$, the problem of finding the capacity $\max\limits_{p_X(\cdot)} \mathrm{I}(X;Y)$ of the discrete print-and-scan channel is more involved. The difficulty arises from the fact that both terms in the right-hand-side of (6) depend on $p_X(\cdot)$.

However, we can follow the same reasoning and notation as in Sect. IV-A and still make use of MLC/MSD in order to approach $\mathrm{I}(X;Y)$. The main difference with respect to the discrete AWGN channel is that the noise Z has a generalized Gaussian distribution with standard deviation and shape factor depending on the channel input X. We show in Figs. 17 and 18 an example of the equivalent channels corresponding to a print-and-scan channel modeled by (2) and (3). For $i = 0, 1, \ldots, L-1$, the

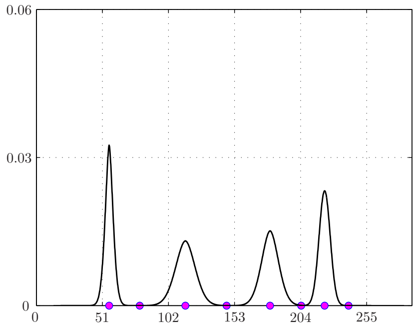

(a)

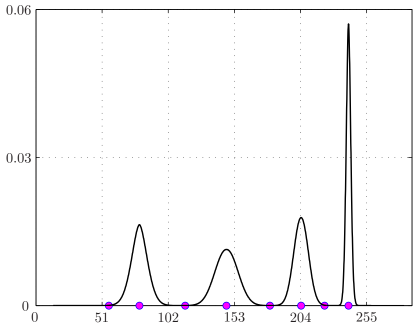

(b)

Fig. 17. Conditional p.d.f.'s for the equivalent channel at level 0 when an 8–PAM non-equidistant constellation with Ungerböck's labeling is used for communications over a print-and-scan channel: (a) $f(y|b^0=0)$, (b) $f(y|b^0=1)$.

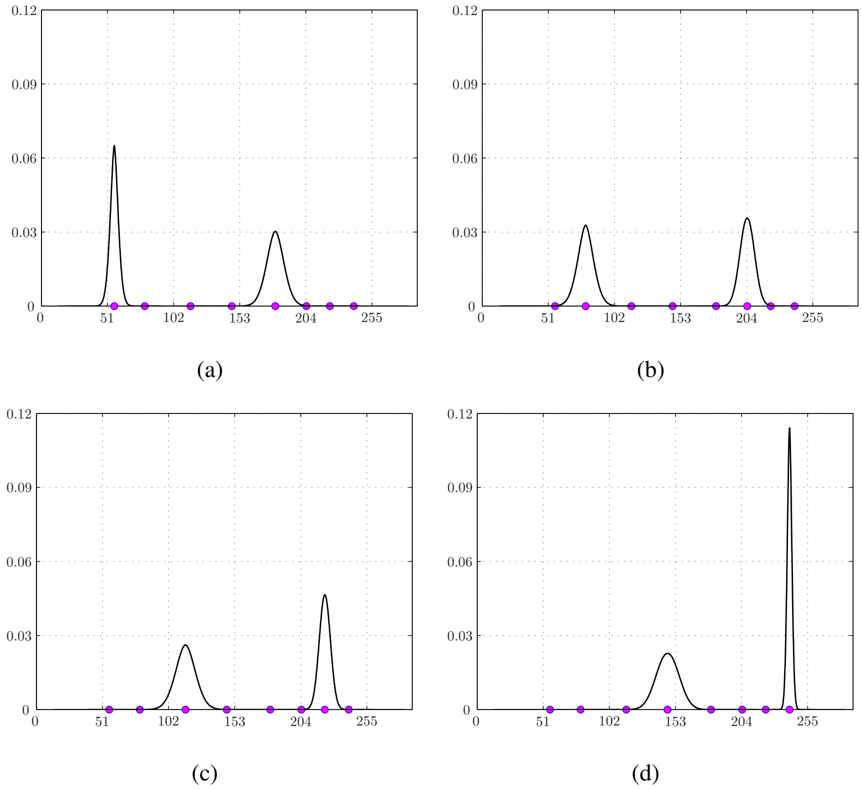

Fig. 18. Conditional p.d.f.'s for the equivalent channel at level 1 when an 8–PAM non-equidistant constellation with Ungerböck's labeling is used for communications over a print-and-scan channel: (a) $f(y|b^1 = 0, b^0 = 0)$, (b) $f(y|b^1 = 0, b^0 = 1)$, (c) $f(y|b^1 = 1, b^0 = 0)$, (d) $f(y|b^1 = 1, b^0 = 1)$.

individual rates R_i of the component codes can be computed as follows:

$$\begin{aligned} R_i &= \mathrm{I}(B^i; Y | B^0, \ldots, B^{i-1}) \\ &= \mathrm{h}(Y|B^0, \ldots, B^{i-1}) - \mathrm{h}(Y|B^0, \ldots, B^{i-1}, B^i). \end{aligned} \tag{9}$$

We compute the term $\mathrm{h}(Y|B^0, \ldots, B^{i-1})$ in (9) as follows. By definition:

$$\mathrm{h}(Y|B^0, \ldots, B^{i-1}) = \sum_{(b^0,\ldots,b^{i-1}) \in \mathcal{B}^i} \mathrm{h}(Y|B^0 = b^0, \ldots, B^{i-1} = b^{i-1}) p(b^0, \ldots, b^{i-1}),$$

and

$$\mathrm{h}(Y|B^0 = b^0, \ldots, B^{i-1} = b^{i-1}) = -\int_{\mathcal{Y}} f(y|b^0, \ldots, b^{i-1}) \log f(y|b^0, \ldots, b^{i-1}) \, \mathrm{d}y.$$

Hence, in order to compute $\mathrm{h}(Y|B^0 = b^0, \ldots, B^{i-1} = b^{i-1})$ we need to specify $f(y|b^0, \ldots, b^{i-1})$. This can be done by conditioning on $B^i = b^i, \ldots, B^{L-1} = b^{L-1}$:

$$f(y|b^0, \ldots, b^{i-1}) = \sum_{(b^i,\ldots,b^{L-1}) \in \mathcal{B}^{L-i}} f(y|b^0, \ldots, b^{i-1}, b^i, \ldots, b^{L-1}) \cdot p(b^i, \ldots, b^{L-1}).$$

Therefore,

$$f(y|b^0,\ldots,b^{i-1}) = \sum_{(b^i,\ldots,b^{L-1})\in\mathcal{B}^{L-i}} f(y|\psi(b^0,\ldots,b^{L-1}))\cdot p(b^i,\ldots,b^{L-1}).$$

Exactly like for $f(y)$ in (8), $f(y|\psi(b^0,\ldots,b^{L-1}))$ can be obtained noting that $(Y|X=x)\sim\mathcal{GGD}(\varphi(x),\sigma_Z(x),\gamma_Z(x))$. Obviously, we can proceed in the same manner in order to compute the term $\mathrm{h}(Y|B^0,\ldots,B^{i-1},B^i)$ in (9). Notice that since $f(y|\psi(b^0,\ldots,b^{L-1}))$ depends on the actual mapping ψ, R_i in (9) is also *mapping dependent* for $i=0,1,\ldots,L-1$.

V. Experimental Results on the Design of Multilevel 2D Bar Codes Using MLC/MSD

In this section, we exploit the discrete channel model developed in Sect. III-C and the results of Sect. IV-B in order to design practical multilevel 2D bar codes.

A. Constellation and MLC/MSD Rate Design for Communications Over the Print-and-Scan Channel

By using the estimated functions $\varphi(\cdot)$ and $\sigma_Z(\cdot)$, we select a signal constellation $\mathcal{X}$ in such a way that the *received* signal points are close to each other where the noise standard deviation is small and farther apart where the noise standard deviation is large. The actual number of selected constellation points depends on the first- and second-order statistics of the print-and-scan channel and the error-correcting capabilities of the individual codes used for MLC/MSD. The selected non-equidistant 8–PAM signal constellations for the considered combinations of printers and scanners are reported in Table II.

For illustration, we schematize in Fig. 19 the employed algorithm for building the constellation for p_2-s_3. If we define $\Delta=\varphi(255)-\varphi(0)$, then the constellation points and the value of k in this figure can be obtained by solving the following minimization problem:

$$\min_{\substack{x_1,\ldots,x_8\\ k\in\mathbb{R}^+}} \left|\Delta - k\left(\sigma_Z(x_1)+2\sum_{i=2}^{7}\sigma_Z(x_i)+\sigma_Z(x_8)\right)\right|,$$

subject to $x_1<x_2<\ldots<x_8$ and $x_1,\ldots,x_8\in[0,255]$.

In Sect. III-B, we explained how to determine the parameters of the discrete print-and-scan channel model for the selected constellation $\mathcal{X}$. The obtained results for the considered printer and scanner combinations are shown in Fig. 9 and Table III. By using these parameters and following the procedure described in Sect. IV-B, we numerically compute the rates R_i, $i=0,1,2$, of an MLC/MSD scheme employing the signal constellation $\mathcal{X}$, together with Ungerböck's labeling. We show in Table IV the obtained rates.

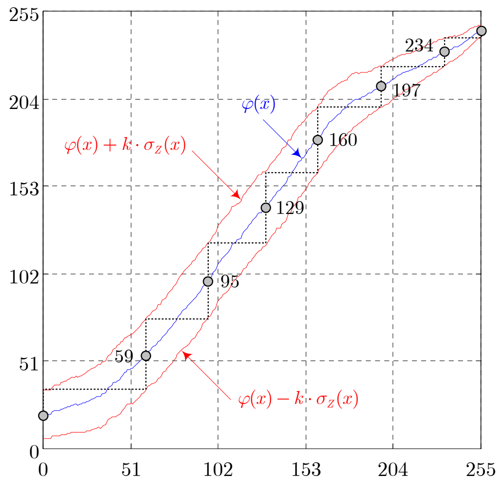

Fig. 19. Building up the non-equidistant 8–PAM signal constellation $\mathcal{X}$ for the $p_2 - s_3$ combination, $k = 1.09$.

B. *Performance Evaluation of Multilevel 2D Bar Codes Using MLC/MSD*

We studied the performance of multilevel 2D bar codes using MLC/MSD for the considered printer and scanner combinations.

For this task, we implemented respectively 15 non-equidistant 8–PAM MLC/MSD schemes using the design parameters obtained in Sect. V-A, namely signal constellations (Table II) and channel model parameters (Table III). For the individual component codes of all MLC/MSD schemes, we used low-density parity-check (LDPC) codes. More precisely, we used the Matlab implementation of *quasi-regular* LDPC codes from I. Kozintsev [27].

A multilevel encoder has a straightforward implementation. For the multistage decoder, one must take into account the statistics of the underlying discrete print-and-scan channel model in order to correctly compute the log-likelihood ratios l_n^i used in the LDPC belief propagation decoding algorithm:

$$l_n^i = \ln \frac{f_{Y|B^i,B^0,\ldots,B^{i-1}}(y_n|1,\hat{b}^0,\ldots,\hat{b}^{i-1})}{f_{Y|B^i,B^0,\ldots,B^{i-1}}(y_n|0,\hat{b}^0,\ldots,\hat{b}^{i-1})}, \qquad i = 0,\ldots,L-1, \qquad n = 1,\ldots,N.$$

The terms $f_{Y|B^i,B^0,\ldots,B^{i-1}}(y_n|b_i,\hat{b}^0,\ldots,\hat{b}^{i-1})$, $b_i = 0,1$, in the last equation, are computed as in Sect. IV-B.

The bit error rate (BER) of the designed multilevel 2D bar codes was evaluated for $R = 2$ bits per 2D symbol or, equivalently, 1121 bytes / in^2. The individual code rates R_i, $i = 0,1,2$, were selected according to the capacity rule for an 8–PAM MLC/MSD scheme with Ungerböck's labeling over an AWGN channel (see first row of Table VI).

TABLE IV

INDIVIDUAL CODE RATES AND TOTAL RATE FOR MULTILEVEL 2D BAR CODES USING MLC/MSD ($N \to \infty$)

	R_0	R_1	R_2	R
$p_1 - s_1$	0.8318	0.9993	1.0000	2.8311
$p_1 - s_2$	0.4153	0.9669	1.0000	2.3822
$p_1 - s_3$	0.3699	0.9213	0.9996	2.2908
$p_2 - s_1$	0.2490	0.9158	1.0000	2.1647
$p_2 - s_2$	0.2083	0.8796	1.0000	2.0880
$p_2 - s_3$	0.2544	0.9019	1.0000	2.1563
$p_3 - s_1$	0.6965	0.9947	1.0000	2.6912
$p_3 - s_2$	0.3244	0.9126	1.0000	2.2370
$p_3 - s_3$	0.2677	0.7200	0.9915	1.9793
$p_4 - s_1$	0.1159	0.7060	0.9968	1.8187
$p_4 - s_2$	0.0827	0.4924	0.9942	1.5693
$p_4 - s_3$	0.1095	0.6699	0.9952	1.7746
$p_5 - s_1$	0.9632	0.9999	1.0000	2.9631
$p_5 - s_2$	0.6286	0.9825	1.0000	2.6110
$p_5 - s_3$	0.8774	0.9992	1.0000	2.8766

TABLE V

BER RESULTS OF MULTILEVEL 2D BAR CODES FOR $R = 2$ ($N = 2048$)

	$Z \sim \mathcal{N}(0, \sigma_Z^2)$		$(Z\|X = x) \sim \mathcal{N}(0, \sigma_Z^2(x))$		$(Z\|X = x) \sim \mathcal{GGD}(0, \sigma_Z(x), \gamma_Z(x))$	
	BER mean	BER variance	BER mean	BER variance	BER mean	BER variance
$p_1 - s_1$	0	0	0	0	0	0
$p_1 - s_2$	2.814×10^{-2}	8.154×10^{-4}	7.641×10^{-6}	9.341×10^{-10}	0	0
$p_1 - s_3$	2.098×10^{-2}	2.178×10^{-4}	0	0	0	0
$p_2 - s_1$	6.703×10^{-2}	2.487×10^{-4}	1.726×10^{-2}	3.284×10^{-4}	1.680×10^{-2}	3.191×10^{-4}
$p_2 - s_2$	7.859×10^{-2}	2.314×10^{-4}	5.084×10^{-2}	3.143×10^{-5}	5.046×10^{-2}	3.177×10^{-5}
$p_2 - s_3$	6.452×10^{-2}	4.429×10^{-4}	1.296×10^{-2}	4.331×10^{-4}	1.052×10^{-2}	2.619×10^{-4}
$p_3 - s_1$	0	0	0	0	0	0
$p_3 - s_2$	1.817×10^{-2}	3.821×10^{-4}	0	0	0	0
$p_3 - s_3$	1.010×10^{-1}	1.280×10^{-4}	4.149×10^{-3}	1.316×10^{-5}	3.744×10^{-3}	1.032×10^{-5}
$p_4 - s_1$	1.356×10^{-1}	3.432×10^{-5}	1.283×10^{-1}	1.943×10^{-5}	1.276×10^{-1}	1.124×10^{-5}
$p_4 - s_2$	1.530×10^{-1}	8.754×10^{-5}	1.563×10^{-1}	4.813×10^{-5}	1.649×10^{-1}	2.800×10^{-5}
$p_4 - s_3$	1.243×10^{-1}	2.478×10^{-5}	1.176×10^{-1}	3.058×10^{-5}	1.168×10^{-1}	4.366×10^{-5}
$p_5 - s_1$	0	0	0	0	0	0
$p_5 - s_2$	0	0	0	0	0	0
$p_5 - s_3$	0	0	0	0	0	0

We present the obtained BER results in Table V. For comparison, three channel models, all derived from (2) and (3), were considered for decoding the multilevel 2D bar codes. The first model assumes stationary Gaussian noise, i.e. $Z \sim \mathcal{N}(0, \sigma_Z^2)$, where:

$$\sigma_Z^2 = \frac{1}{|\mathcal{X}|} \sum_{x \in \mathcal{X}} \sigma_Z^2(x), \;\; \gamma_Z(x) = 2, \;\; \text{for all } x \in \mathcal{X}.$$

The second model assumes luminance-dependent Gaussian noise, meaning that $\gamma_Z(x) = 2$ for all $x \in \mathcal{X}$, but the noise standard deviation $\sigma_Z(x)$ varies for each $x \in \mathcal{X}$. Finally, the third model assumes luminance-dependent generalized Gaussian noise, meaning that noise standard deviation $\sigma_Z(x)$ and shape factor $\gamma_Z(x)$ vary for all $x \in \mathcal{X}$ as shown in Table III.

C. Fine Tuning of Multilevel 2D Bar Codes Using MLC/MSD

From the results in Tables IV and V, we observe that the best and worst combinations of *laser* printer and scanner are, respectively, $p_1 - s_1$ and $p_4 - s_2$. We notice also that the inkjet printer and scanner combination $p_5 - s_1$ is the most attractive since it gives the best results in terms of achievable rate R. In this section, we investigate the practical performance limits of multilevel 2D bar codes for the best combinations $p_1 - s_1$ and $p_5 - s_1$[6].

We evaluated the performance of the designed multilevel 2D bar codes for different embedding rates R (in bits / 2D symbol). For each embedding rate R, the individual code rates R_i, $i = 0, 1, 2$, were selected by using the capacity rule for an 8–PAM MLC/MSD scheme with Ungerböck's labeling over an AWGN channel. However, we did not use this selection rule for the embedding rates $R = 2.8311$ and $R = 2.9631$ which correspond to the rates in the first and thirteenth rows of Table IV. For a block length of $N = 2048$ bits at all levels, the corresponding generator and parity-check matrices were generated randomly according to these rates. Nevertheless, due to a limitation of the employed software package, we were not able to generate these matrices for very high rates, i.e. for rates R_i such that $0.9951 \leq R_i < 1$. For these cases, $R_i = 1$ was taken. We summarize in Table VI the selected parameters for multilevel coding. Therein, we have $R_i \approx K_i/N$. The numbers in parentheses correspond to the cases where R_i was rounded up to 1.

We present the obtained BER results in Tables VII and VIII.

[6]We do not investigate further the worst combination $p_4 - s_2$ because for this case the gain in terms of storage capacity of multilevel 2D bar codes with respect to B&W 2D bar codes would be minor (see Tables IV and IX).

TABLE VI

SELECTED PARAMETERS FOR MULTILEVEL CODING ($N = 2048$)

R	R_0	R_1	R_2	K_0	K_1	K_2
2.0	0.1747	0.8231	0.9996	357	1685	(2048)
2.4	0.4279	0.9694	1.0000	876	1985	2048
2.5	0.5106	0.9837	1.0000	1045	2014	2048
2.6	0.6068	0.9930	1.0000	1242	2033	2048
2.7	0.6992	0.9975	1.0000	1431	(2048)	2048
2.8311	0.8318	0.9993	1.0000	1703	(2048)	2048
2.9631	0.9632	0.9999	1.0000	1972	(2048)	2048

TABLE VII

BER RESULTS OF MULTILEVEL 2D BAR CODES FOR THE $p_1 - s_1$ COMBINATION ($N = 2048$)

R	bytes / in^2	$Z \sim \mathcal{N}(0, \sigma_Z^2)$	$(Z\|X = x) \sim \mathcal{N}(0, \sigma_Z^2(x))$	$(Z\|X = x) \sim \mathcal{GGD}(0, \sigma_Z(x), \gamma_Z(x))$
2.4	1346	0	0	0
2.5	1400	1.909×10^{-3}	8.567×10^{-5}	3.671×10^{-5}
2.8311	1590	4.640×10^{-2}	3.973×10^{-2}	3.930×10^{-2}
3.0	1684	5.012×10^{-2}	4.146×10^{-2}	4.121×10^{-2}

The last rows in Tables VII and VIII correspond to the performance results of the *uncoded* version of the designed multilevel 2D bar codes. For this case, maximum likelihood detection was employed along with the above three channel models.

From Table VIII, we observe that for the stationary and luminance-dependent Gaussian noise models, the performance of the multistage decoder is quite similar. This is in agreement with Fig. 8(m), where we can see that for the $p_5 - s_1$ combination the noise standard deviation is approximately constant.

TABLE VIII

BER RESULTS OF MULTILEVEL 2D BAR CODES FOR THE $p_5 - s_1$ COMBINATION ($N = 2048$)

R	bytes / in^2	$Z \sim \mathcal{N}(0, \sigma_Z^2)$	$(Z\|X = x) \sim \mathcal{N}(0, \sigma_Z^2(x))$	$(Z\|X = x) \sim \mathcal{GGD}(0, \sigma_Z(x), \gamma_Z(x))$
2.6	1459	0	0	0
2.7	1515	3.392×10^{-5}	3.392×10^{-5}	1.131×10^{-5}
2.9631	1663	4.985×10^{-3}	3.296×10^{-3}	2.874×10^{-3}
3.0	1684	5.229×10^{-3}	3.855×10^{-3}	3.866×10^{-3}

However, this equivalence in performance is not expected when the noise standard deviation varies (see for example Fig. 8(a) and Table III(a)). Indeed, we observe from the second row of Table VII that for the $p_1 - s_1$ combination the luminance-dependent Gaussian noise model provides a substantial gain in performance with respect to the stationary Gaussian noise model. Tables V, VII and VIII also show that the performance of the multistage decoder when using the luminance-dependent generalized Gaussian noise model is in almost all cases better than those obtained for the two other noise models.

Concerning the next to last rows in Tables VII and VIII, which correspond to the theoretical maximum achievable rates of the proposed modulation schemes, we think that the main reasons explaining the marginal advantage of the multistage decoder with respect to the uncoded version (last row) are twofold. First, the blocklength N of the underlying codes is simply too small. Second, there is no guarantee that the randomly selected parity-check matrices used for multistage decoding show good performance for the considered individual rates (see Table VI).

Notice that the results in Tables VII and VIII were obtained for a suboptimal choice of the modulation scheme. Indeed, the demodulator processes only 44.4% of a received 2D symbol and the space between 2D symbols, although necessary to avoid ISI, was not optimized. Therefore, there is clearly room for improving the proposed multilevel 2D bar codes in terms of both BER and storage capacity. For example, we obtained a 64.5% storage capacity increase by using the following modulation parameters: 6×6 pixel 2D symbols, 1 pixel of inter-symbol space, and $r_{im} = 600$ ppi. This scheme uses the *same* physical size for the 2D symbols but reduces the physical inter-symbol space to a third of the previous one (see Fig. 20). In Table IX, we report the storage capacities (at zero BER) of two multilevel 2D bar codes

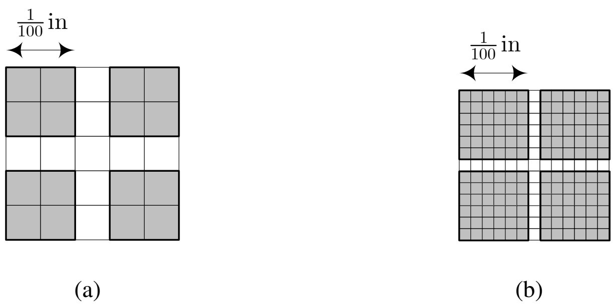

Fig. 20. Modulation parameters for multilevel 2D bar codes. (a) 2×2 pixel 2D symbols, 1 pixel of inter-symbol space, $r_{im} = 200$ ppi. (b) 6×6 pixel 2D symbols, 1 pixel of inter-symbol space, $r_{im} = 600$ ppi.

employing this modulation scheme. For comparison purposes, we also show the public domain 2D bar codes with the highest storage capacities. Surprisingly, these results were obtained by keeping the same constellations shown in Table II and only by recomputing the channel model parameters in Tables III(a) and III(m). In fact, the improvement in storage capacity came for free thanks to the used demodulation algorithm which neglects border pixels and thus provides some resistance to ISI.

TABLE IX

HIGH CAPACITY 2D BAR CODES

Name	bytes / in^2
Data Matrix	1555
Aztec Code	1888
QR Code	1941
Multilevel 2D Bar Code $(p_1 - s_1)$	2211
Multilevel 2D Bar Code $(p_5 - s_1)$	2397

VI. CONCLUSIONS AND FUTURE WORK

In this work, we highlighted the attractiveness of multilevel 2D bar codes for high capacity storage applications. We have also shown how to apply MLC/MSD, originally developed for the AWGN channel, to the print-and-scan channel in the context of multilevel 2D bar codes. A key point is the construction of a simplified model of the print-and-scan channel specifically adapted for this application. This model assumes no ISI and perfect synchronization, but it takes into account the dependence between the channel input and the noise. Our approach can be applied to other printing and reading devices as well as to enhance existing B&W 2D bar codes.

The experimental results show that, in comparison to other public domain 2D bar codes, the storage capacities of the designed multilevel 2D bar codes are among the highest. Therefore, we conclude that multilevel 2D bar codes are very promising candidates to meet the high capacity storage requirements of many new multimedia security and data management applications.

In future work, we plan to investigate the synchronization problem for print-and-scan channels in the context of multilevel 2D bar codes. A good synchronization algorithm would lead to a performance improvement in terms of BER. We also plan to use *irregular* LDPC codes (instead of quasi-regular ones) and larger block lengths to improve the multistage decoder performance. One may also improve the BER performance by considering skewed and non-skewed family distributions for modeling the noise distribution of the discrete print-and-scan channel. Finally, given that a significant improvement in terms of storage capacity may be obtained by eliminating the space between 2D symbols, a more general framework including ISI cancelation is to be investigated.

ACKNOWLEDGMENTS

The authors are thankful to the members of the Stochastic Image Processing group at Geneva University for many helpful and interesting discussions. They also acknowledge the anonymous reviewers for their useful remarks and suggestions which considerably enhanced the technical content of this paper.

REFERENCES

[1] V. N. Kadan, A. S. Pekarik, and R. V. Estrela Liopis, "Dynamic mask: new approach to laser engraving of halftone images," in *Proceedings of the SPIE, Vol. 2993, Lasers as Tools for Manufacturing II*, Apr. 1997, pp. 98–105.

[2] T. Lamarque, R. Nicolaus, B. Loiseaux, J.-P. Huignard, G. Slekys, and J. Xu, "Programmable 2D laser marking device based on a pulsed UV image coherent amplifier," in *Proceedings of the SPIE, Vol. 5063, Fourth International Symposium on Laser Precision Microfabrication*, Nov. 2003, pp. 386–388.

[3] France Telecom R&D, "M-commerce, an emerging sector," http://www.francetelecom.com/sirius/rd/en/ddm/en/technologies/ddm200405/print_index1.htm, May 2004, available by Nov. 1st, 2005.

[4] Symbol Technologies, Inc., "Enterprise Mobility Solutions Deliver Increased Efficiency and Security to Parcel & Post Operations," http://www.symbol.com/products/whitepapers/sbl_dlvrs_efficiency_to_post.html, May 2004, available by Nov. 1st, 2005.

[5] S. Voloshynovskiy, O. Koval, F. Deguillaume, and T. Pun, "Visual communications with side information via distributed printing channels: extended multimedia and security perspectives," in *Proceedings of SPIE Photonics West Electronic Imaging 2004, Multimedia Processing and Applications*, San Jose, USA, Jan. 18-22 2004.

[6] D. Kirovski, N. Jojic, and G. Jancke, "Tamper-Resistant Biometric IDs," in *Information Security Solutions Europe*, Berlin, Germany, Sept. 28-30 2004.

[7] I. Blake, G. Seroussi, and N. Smart, *Elliptic Curves in Cryptography*, ser. Lecture Note Series, London Mathematical Society, Ed. Cambridge University Press, 2000, vol. 265.

[8] J. Fridrich, "Visual Hash For Oblivious Watermarking," in *Proceedings of SPIE Photonic West Electronic Imaging 2000, Security and Watermarking of Multimedia Contents*, vol. 3971, San Jose, California, Jan. 24-26 2000, pp. 286–294.

[9] F. Deguillaume, S. Voloshynovskiy, and T. Pun, "Secure hybrid robust watermarking resistant against tampering and copy-attack," *Elsevier Signal Processing*, vol. 83, no. 10, pp. 2133–2170, Oct. 2003.

[10] D. L. Lau and G. R. Arce, *Modern Digital Halftoning*. New York - Basel: Marcel Dekker, Inc., 2001.

[11] A. K. Jain, *Fundamentals of Digital Image Processing*. Prentice-Hall International, Inc., 1989.

[12] N. Degara-Quintela and F. Pérez-González, "Visible Encryption: Using Paper as a Secure Channel," in *Proceedings of SPIE-IS&T Electronic Imaging 2003: Security and Watermarking of Multimedia Contents V*, vol. 5020, 2003, pp. 413–422.

[13] S. Mallat, "A Theory for Multiresolution Signal Decomposition: The Wavelet Representation," *IEEE Transactions on PAMI*, vol. 11, no. 7, pp. 674 – 693, July 1989.

[14] U. Wachsmann, R. F. H. Fischer, and J. B. Huber, "Multilevel Codes: Theoretical Concepts and Practical Design Rules," *IEEE Transactions on Information Theory*, vol. 45, no. 5, pp. 1361–1391, July 1999.

[15] J. L. Massey, "Coding and Modulation in Digital Communications," in *Proceedings of Intern. Zürich Seminar on Digital Communications*, 1974, pp. E2(1)–E2(4).

[16] G. Forney and G. Ungerboeck, “Modulation and Coding for Linear Gaussian Channels,” *IEEE Transactions on Information Theory*, vol. 44, no. 6, pp. 2384–2415, Oct. 1998.

[17] H. Imai and S. Hirakawa, “A New Multilevel Coding Method Using Error-Correcting Codes,” *IEEE Transactions on Information Theory*, vol. 23, pp. 371–377, May 1977.

[18] U. Wachsmann, “Coded Modulation: Theoretical Concepts and Practical Design Rules,” Ph.D. dissertation, Technischen Fakultät der Universität Erlangen-Nürnberg, July 1999.

[19] U. Wachsmann and J. Huber, “Power and Bandwidth Efficient Digital Communication Using Turbo Codes in Multilevel Codes,” *European Transactions on Telecommunications (ETT)*, vol. 6, pp. 557–567, Sept.-Oct. 1995.

[20] J. Hou, P. H. Siegel, L. B. Milstein, and H. D. Pfister, “Capacity-Approaching Bandwidth-Efficient Coded Modulation Schemes Based on Low-Density Parity-Check Codes,” *IEEE Transactions on Information Theory*, vol. 49, no. 9, pp. 2141–2155, Sept. 2003.

[21] G. Caire, G. Taricco, and E. Biglieri, “Bit-Interleaved Coded Modulation,” *IEEE Transactions on Information Theory*, vol. 44, pp. 927–946, May 1998.

[22] ——, “Capacity of bit-interleaved channels,” *Electronic Letters*, vol. 32, pp. 1060–1061, June 1996.

[23] K. R. Narayanan and J. Li, “Bandwidth Efficient Low Density Parity Check Coding using Multi Level Coding and Iterative Multi Stage Decoding,” in *Proceedings of the International Symposium on Turbo Codes*, Brest, France, Sept. 2000.

[24] P. A. Martin and D. P. Taylor, “On Multilevel Codes and Iterative Multistage Decoding,” *IEEE Transactions on Communications*, vol. 49, no. 11, pp. 1916–1925, Nov. 2001.

[25] S. ten Brink, G. Kramer, and A. Ashikhmin, “Design of Low-Density Parity-Check Codes for Modulation and Detection,” *IEEE Transactions on Communications*, vol. 52, no. 4, pp. 670–678, Apr. 2004.

[26] T. Cover and J. Thomas, *Elements of Information Theory*. John Wiley & Sons, Inc., 1991.

[27] I. Kozintsev, “Matlab programs for encoding and decoding of LDPC codes over GF(2^m),” http://www.kozintsev.net/soft.html, available by May 17th, 2005.

LIST OF FIGURES

List of Tables